Journal of Materials Chemistry A

ROYAL SOCIETY OF CHEMISTRY

PAPER

View Article Online
View Journal | View Issue

Check for updates

Cite this: J. Mater. Chem. A, 2025, 13, 4994

In situ Mo doping in NiS_2: enhancing electron density and stimulating electronic conductivity of Cu_3P–GDY for efficient photocatalytic hydrogen evolution

Jieyuan Du,[a] Fei Jin, *[a] Youji Li,[b] Guoping Jiang*[a] and Zhiliang Jin *[a]

The electronic conductivity of a catalyst can be enhanced by strategically doping with specific elements. In this study, a $Mo_{0.1}NiS_2/Cu_3P$–GDY composite photocatalyst featuring a hierarchical structure was meticulously designed, optimizing the charge migration path to boost electronic conductivity. The *in situ* doping of molybdenum (Mo) induced a Burstein–Moss effect, effectively enhancing the electronic conductivity and electron density of NiS_2. The $Mo_{0.1}NiS_2$ component was paired with a co-catalyst that further stimulated the electronic conductivity of Cu_3P–GDY and expedited electron transport. The findings revealed that the hydrogen evolution capacity of the composite catalyst was 2.9 and 4.7 times greater than those of $Mo_{0.1}NiS_2$ and Cu_3P–GDY, respectively, reaching 133.1 μmol g^{-1}. *In situ* X-ray photoelectron spectroscopy (XPS) and density functional theory (DFT) calculations confirmed the formation of an S-scheme heterojunction between the catalysts, establishing a directional charge transfer pathway that significantly improves the charge transfer rate and, consequently, the hydrogen evolution activity of the composite photocatalyst. This research provides a valuable design strategy for enhancing the hydrogen evolution activity of photocatalysts by increasing electronic conductivity.

Received 23rd October 2024
Accepted 7th January 2025

DOI: 10.1039/d4ta07562e

rsc.li/materials-a

Published on 27 Januwari 2025. Downloaded on 5/28/2026 5:22:55 AM.

1. Introduction

As the world continues to develop, the concept of green sustainable development has gradually gained traction in the minds of people everywhere. Currently, the replacement of traditional energy sources with cleaner ones is a top priority in green sustainable development.[1,2] Hydrogen energy as a green and high-calorific value clean energy source is the optimal replacement for fossil energy sources. Using solar energy as a driving force to decompose water into hydrogen through a catalytic reaction is an ideal way to produce hydrogen.[3,4] However, the significant recombination of charge and the inadequate hydrogen evolution kinetics among the catalysts result in the limited applicability of this technology at a large scale.[5,6] Concurrently, the single catalyst often lacks a directional electric field, which results in the random transport of the photogenerated electrons and photogenerated holes within the catalyst.[7,8] Therefore, the separation and transport performance of the electrons can be enhanced by doping, supporting cocatalysts and constructing heterojunctions, while the side reactions between photogenerated carriers and photogenerated holes can be reduced.[9,10] In order to increase the photogenic charge involved in the photocatalyst surface reaction, the heterojunctions were constructed *via* structural design to optimize the charge transport within the catalyst.

The narrow band gap of metal chalcogenides makes them an advantageous material for use in solar energy collection. However, NiS_2 has poor stability.[11] The performance of catalysts is frequently enhanced by means of techniques such as increasing crystallinity and elemental doping.[12,13] Consequently, the Mo element with a larger atomic radius was incorporated to enhance the stability of NiS_2.[14,15] The doping of the Mo element is conducive to improving the energy band structure, which enhances the electronic conductivity of NiS_2 and thus accelerates the electron transfer. Furthermore, the construction of a heterojunction between nickel disulfide and other semiconductors is favored, which improves the separation efficiency of the photogenerated carriers and positively promotes photocatalytic hydrogen evolution. Nevertheless, the narrow band gap between $Mo_{0.1}NiS_2$ is not conducive to the efficient use of photogenic carriers.

In order to enhance the efficiency of the utilization of the $Mo_{0.1}NiS_2$ photogenerated carriers, an organic catalyst with a narrow band gap was introduced. In recent years, there has been a notable advancement in the utilization of organic catalysts in the domain of photocatalysis, with carbon materials

[a]School of Chemistry and Chemical Engineering, Ningxia Key Laboratory of Solar Chemical Conversion Technology, Key Laboratory for Chemical Engineering and Technology, State Ethnic Affairs Commission, North Minzu University, Yinchuan 750021, P. R. China. E-mail: jinfei@nmu.edu.cn; jiangguoping-6609@163.com
[b]College of Chemistry and Chemical Engineering, Jishou University, Jishou, Hunan 416000, PR China. E-mail: zl-jin@nun.edu.cn

This journal is © The Royal Society of Chemistry 2025

Published on 27 Januwari 2025. Downloaded on 5/28/2026 5:22:55 AM.

exhibiting a particularly rapid evolution in this regard. Among the new carbon materials, graphdiyne (GDY) is emerging as a promising candidate owing to its stability and conductivity.[16,17] GDY, a two-dimensional (2D) material comprising sp and sp^2 hybrid carbon atoms, has demonstrated considerable potential in the fields of photocatalysis and electrocatalysis.[18,19] Its uniform pore structure enables the formation of a greater number of adsorption sites for metal ions, thereby facilitating the acceleration of electron transfer.[20,21] The synthesis of Cu_3P–GDY was finally achieved in this work by successfully anchoring Cu^+ to the surface of GDY *via* an *in situ* copper surface-mediated synthesis method. Upon adsorption of copper ions on the surface of GDY, the d orbital of Cu^+ will form a strong interaction with the p orbital of C≡C in GDY,[22,23] when the binding of the negatively charged P element to the Cu ion will result in the Cu metal ion acquiring a higher oxidation state.[24] The electronic structure of the metal is regulated by the interaction of electrons, which enhances the reactivity of the catalyst. Simultaneously, $Mo_{0.1}NiS_2$ with a higher electron density can further enhance the electronic conductivity of Cu_3P–GDY, thereby optimizing the hydrogen evolution performance of the composite catalyst.

In this work, $Mo_{0.1}NiS_2$ with high electronic conductivity was synthesized by *in situ* doping of the Mo element. The doping of the Mo element improves the electron conductivity and electron density of the catalyst. By introducing the cocatalyst Cu_3P–GDY, the problem of the high recombination rate of the $Mo_{0.1}NiS_2$ carrier is solved, which also stimulated an enhancement in the conductivity of Cu_3P–GDY. The close contact between Cu_3P–GDY and $Mo_{0.1}NiS_2$ provides more hydrogen evolution active sites and reactant adsorption sites for the composite photocatalyst. At the same time, the heterojunction formed between the new composite photocatalysts optimizes the separation rate and migration path of the photogenerated carriers. The experimental results show that its excellent catalytic performance can promote the hydrogen evolution of photocatalysts. The results of characterization and DFT theoretical calculation show that the excellent catalytic properties are due to the excellent charge transport between interfaces.

2. Experimental

2.1. Materials

Analytical-grade chemicals were used during the catalyst synthesis. Trimethylsilylacetylene ($C_5H_{10}Si$, Energy Chemical, AR ≥ 98.0%), cobalt(II) nitrate hexahydrate ($Ni(NO_3)_2 \cdot 6H_2O$, 3A (Alab Anhui), AR ≥ 98%), pyridine (C_5H_5N, Energy Chemical, AR ≥ 99.5%), sodium molybdate dihydrate ($Na_2MoO_4 \cdot 2H_2O$, 3A (Alab Anhui), AR ≥ 99.99%), sodium hypophosphite monohydrate ($NaH_2PO_2 \cdot H_2O$, Energy Chemical, 98.0%), sodium sulfide hydrate, ($Na_2S \cdot 9H_2O$, Energy Chemical, AR ≥ 98.0), zinc chloride ($ZnCl_2$, Energy Chemical, AR ≥ 98.0%), hexabromobenzene (C_6Br_6, Macklin, AR ≥ 99.0%), tetrabutylammonium fluoride ($C16H_{36}FN$, Energy Chemical, 1.0 mol L^{-1} in THF), *n*-butyllithium (C_4H_9Li, Energy Chemical, 1.6 mol L^{-1} in hexane), tetrakis(triphenylphosphine)palladium ($Pd(PPh_3)_4$, Energy Chemical, ≥99.0%), tetrahydrofuran (C_4H_8O, Energy Chemical, AR ≥ 99.5%), and hydrochloric acid (HCl, SCR, 36.0–38.0%) were used.

2.2. Synthesis of Cu_3P–GDY

The synthesis of Cu_3P–GDY was achieved through *in situ* copper surface-mediated synthesis, as shown in Fig. 1(a). A 4.3 mL of trimethylsilylene was dissolved in 40 mL of tetrahydrofuran by mixing. The protective agent *n*-butyllithium was added during the low-temperature reaction (−78 °C) for 30 min, followed by the addition of 20 mL of anhydrous zinc chloride for 30 min to obtain trimethylsilyl zinc chloride. Once the mixed solution had reached room temperature, appropriate amounts of hexabromobenzene, tetra-rake powder and toluene solution were added in a sequential manner. Subsequently, the reaction was placed in an oxygen-free environment for a period of 72 h at a temperature of 80 °C. At the conclusion of the reaction, hydrochloric acid and ethyl acetate were added for extraction, and the solution was subsequently washed on multiple occasions with saline and deionized water. Subsequently, the solution was dried with anhydrous sodium sulfate, after which it was concentrated to obtain a light yellow trimethylsilyl alkynyl. Tetrabutylammonium fluoride and tetrahydrofuran were added to remove the silyl group to obtain hexaethynylbenzene. Then, 75 mL of pyridine and Cu powder were added, and the reaction was carried out at 60 °C for 48 h. After the reaction, Cu–GDY was reacted with sodium hypophosphite in a muffle furnace at 400 °C for 4 h to obtain Cu_3P–GDY.

2.3. Synthesis of composite photocatalyst Mo–NiS_2/Cu_3P–GDY

The catalyst Mo–NiS_2 was prepared by the cation exchange method as shown in Fig. 1(b). Initially, 0.1 mmol Na_2MoO_4,

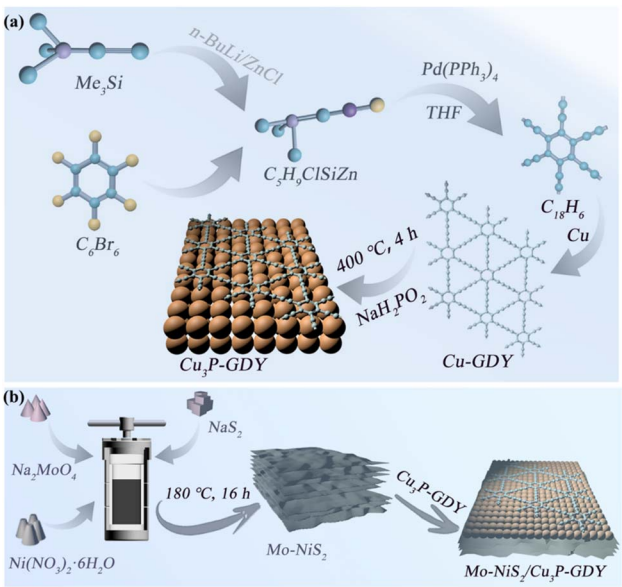

Fig. 1 Schematic diagram of the Cu_3P–GDY synthesis route (a) and the composite photocatalyst CGM-*X* (*X* = 5, 10, 15, and 20) synthesis route (b).

Published on 27 Januwari 2025. Downloaded on 5/28/2026 5:22:55 AM.

1 mmol $Ni(NO_3)_2 \cdot 6H_2O$ and 4 mmol $Na_2S \cdot 9H_2O$ were dissolved in 80 mL deionized water. Following ultrasonication for 30 min, 2 mL of CH_3COOH was added after continuous stirring for 2 h. The stirring was continued for a further 30 min. The solution was transferred to a 100 mL Teflon-lined stainless steel reactor and reacted at 180 °C for 16 h. At the end of the reaction, the solution was washed with deionized water and ethanol alternately several times. Subsequently, it was placed in an oven at 80 °C for drying to finally obtain Mo–NiS_2. The composite photocatalyst CGM-10 was obtained by weighing 50 mg of Mo–NiS_2 and 5 mg of Cu_3P–GDY and mixing them in 30 mL of an ethanol solution. Following a reaction period of three hours, the mixture was transferred to a water bath for drying, and the composite photocatalyst CGM-*X* (*X* represents the weight ratio between Cu_3P–GDY and $Mo_{0.1}NiS_2$). When the ratio of Cu_3P–GDY to $Mo_{0.1}NiS_2$ is 1 : 10, the value of *X* is 10 ($X = 5$, 15, or 20) was obtained.

2.4. Hydrogen evolution experiment

All experiments pertaining to the photocatalytic hydrogen evolution were conducted in a 5 W simulated channel. Firstly, 9 mg of the photocatalyst and 9 mg of eosin Y (EY) were uniformly dispersed into a 30 mL solution of triethanolamine (TEOA, 15%) to form a homogeneous suspension. Subsequently, following the transfer of the mixed suspension solution to the hydrogen evolution bottle, nitrogen was injected to purge for a period of 5 min in order to remove the air present within the bottle. Hydrogen was extracted 5 mL per hour and injected into a gas chromatograph (Tianmie GC7900, TCD, 13X column) using nitrogen as the carrier gas in order to analyze the hydrogen present in the photocatalytic hydrogen evolution process.

2.5. Characterization

The XRD pattern of the photocatalyst was recorded using copper Kα ($\lambda = 1.54$) radiation in an X-ray diffractometer. The internal structure of GDY was tested by Raman spectroscopy and Fourier transform infrared spectroscopy. The surface morphology of each photocatalyst was analyzed by scanning electron microscopy (SEM), while the elemental composition of the catalyst was analyzed by energy-dispersive X-ray spectroscopy (EDS). The electrochemical and optical properties of the catalysts were analyzed using electrochemical workstations and fluorescence spectrometers, respectively. The elemental composition and valence distribution of the catalyst were analyzed by X-ray photoelectron spectroscopy. In addition, the binding energy was calibrated using C 1s (284.8 eV) as a reference.

2.6. Electrochemical test procedure

The light source employed in our electrochemical experiments was a 300 W xenon lamp with a wavelength range of 320–780 nm. In the course of testing IT, EIS and LSV, 5 mg of catalyst was dissolved in 300 μL of 10% Dupont membrane solution and applied to a 1 × 2 conductive glass sheet. Concurrently, a 15% $NaSO_3$ solution was utilized as an electrolyte.

3. Results and discussion

3.1. Structure analysis of photocatalysts

Firstly, the successful preparation of GDY was demonstrated by the corroboration of X-ray diffraction (XRD), infrared (IR) and Raman spectroscopy. From Fig. 2(a), a broad diffraction peak was observed near 23° for GDY, which is an amorphous organic compound.[25] In order to further elucidate the internal structure

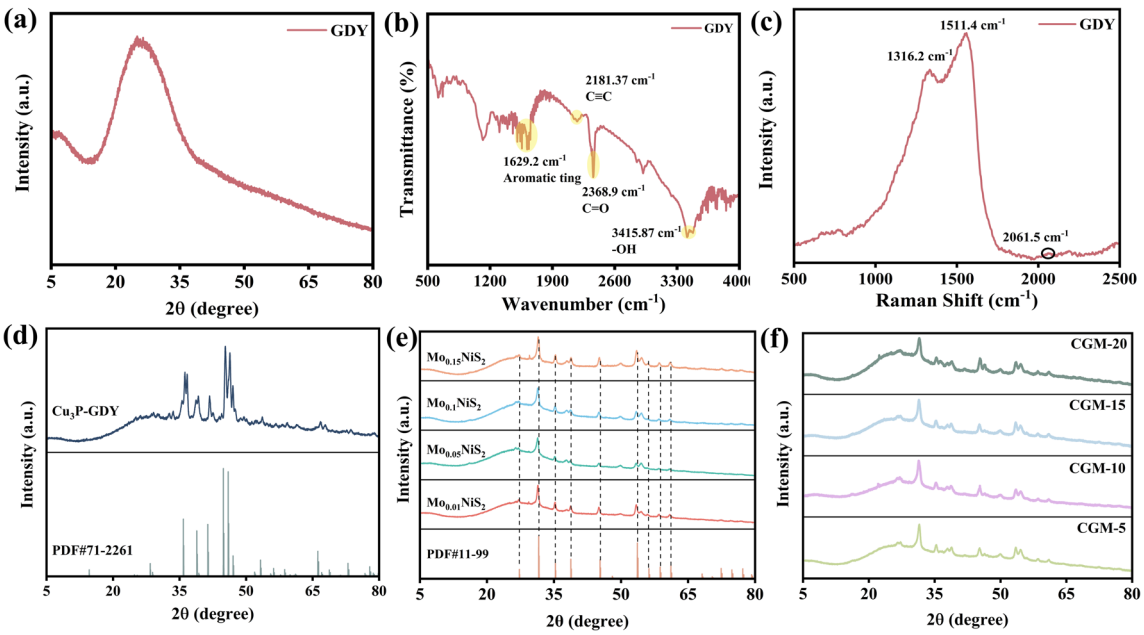

Fig. 2 (a) XRD pattern, (b) FTIR, and (c) Raman spectra of GDY. XRD patterns of (d) Cu_3P–GDY (e) NiS_2 with different proportions of Mo doping, and composite photocatalysts with different Cu_3P–GDY ratios; (f) different Cu_3P–GDY ratios in composite catalysts.

 This journal is © The Royal Society of Chemistry 2025

Published on 27 Januwari 2025. Downloaded on 5/28/2026 5:22:55 AM.

of GDY, IR and Raman tests were conducted on GDY. A weak peak at 2181.4 cm^{-1}, indicative of the stretching vibration of C≡C, was identified, as shown in Fig. 2(b). Concurrently, the characteristic stretching vibration peak of the aromatic ring was observed at 1629.2 cm^{-1}.[26] These findings substantiated the hypothesis that GDY is a mesh structure constituted by the interconnection of sp and sp^2 carbon atoms. Nevertheless, the maximum at 3415.8 cm^{-1} can be attributed to the adsorption of minute quantities of water molecules in the air by the catalyst. Furthermore, the test of Raman spectra in Fig. 2(c) revealed the presence of D-band peaks (1316.2 cm^{-1}), G-band peaks (1511.4 cm^{-1}) and C≡C peaks (2061.5 cm^{-1}), which are indicative of the vibrations of different functional groups.[27] Among the observed peaks, the D-band and G-band peaks are attributed to first-order Raman scattering processes.[28] The D-band peak is due to the respiratory vibration of the sp^2 carbon under the E_{2g} mode scattering, while the G-band peak is due to the stretching vibration of the sp^2 carbon in the benzene ring.[29] The characterization results are sufficient to demonstrate that GDY was successfully synthesized.

The phase compositions of all the catalysts were then characterized and analyzed by XRD. Fig. 2(d) illustrates that Cu_3P–GDY corresponds to hexagonal Cu_3P (PDF # 74-1067). Simultaneously, as shown in Fig. 2(e), the $Mo_{0.1}NiS_2$ diffraction peaks for different Mo doping ratios show a blue shift compared to the cubic NiS_2 structure (PDF # 11-99). This shift is attributed to the larger atomic radius of Mo atoms (145 pm) compared to that of Ni atoms (135 pm). When NiS_2 was doped with the element Mo, it was observed that all peaks were shifted to a lower angle.[30] Furthermore, the introduction of Mo into NiS_2 results in the formation of additional defect sites on the catalyst surface, which facilitate the separation and adsorption of water.[31,32] When the main catalyst is introduced into a cocatalyst, the crystal structure of individual catalysts is often affected. Fig. 2(f) demonstrates that as the content of Cu_3P–GDY in the composite catalyst CGM increases, the peak value of Cu_3P at 36° and 46° increases.

The morphology and structure of the catalysts were scrutinized using SEM and high-resolution TEM (HRTEM). Fig. 3(a) shows the larger layered structure of $Mo_{0.1}NiS_2$ with a diameter of about 3.38 ± 1.35 μm. Fig. 3(b) shows the surface of Cu_3P–GDY exhibiting a blocky structure with a diameter of about 151.57 ± 62.91 nm. Smaller cubes of Cu_3P–GDY are attached to the layered $Mo_{0.1}NiS_2$ surface by the attraction between electrons (Fig. 3(c)). The interconnection of $Mo_{0.1}NiS_2$ and Cu_3P–GDY enables the formation of heterojunctions, facilitating electron transport. Additionally, Cu_3P–GDY provides more active sites for hydrogen evolution. Fig. 3(d) shows the electron transmission diagram of CGM-10, and the distribution of elements in CGM is analyzed by EDX. As expected, C, Cu and P are evenly distributed on the surface of $Mo_{0.1}NiS_2$. ICP-MS analysis of $Mo_{0.1}NiS_2$ was carried out to determine the elemental content of Mo. The test results are basically in agreement with the experimental results. The HRTEM image of CGM-10 (Fig. 3(f)) reveals that the lattice of Mo doped with NiS_2 is distorted. It is well known that lattice defects can promote the

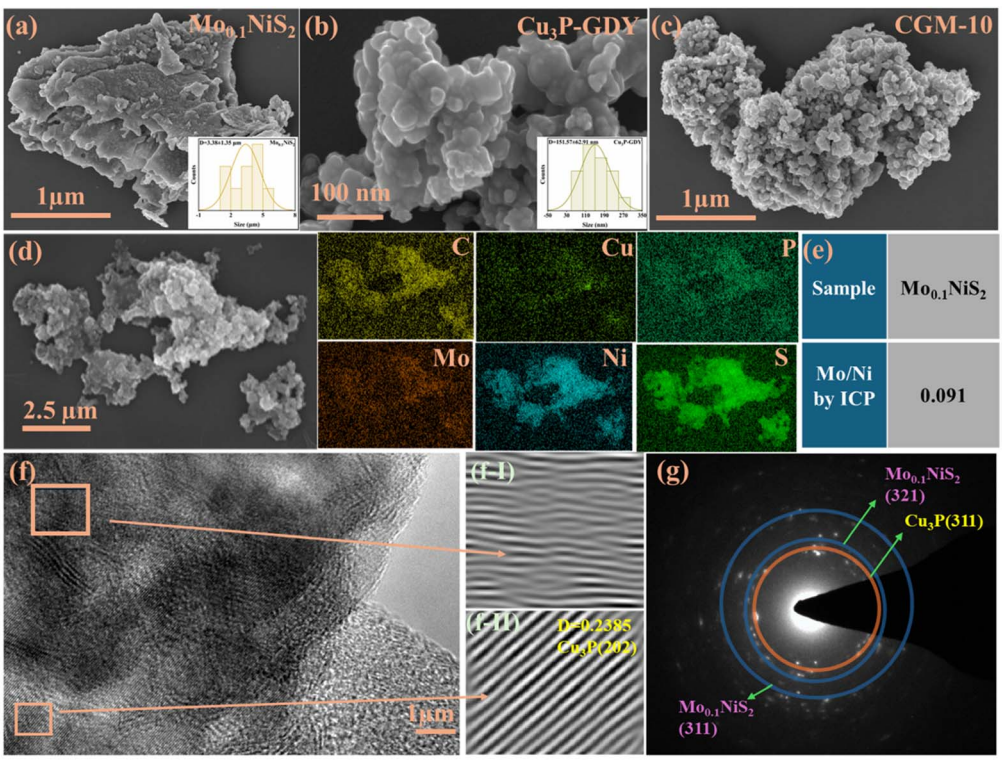

Fig. 3 (a) and (b) Are the SEM and particle size distribution diagrams of $Mo_{0.1}NiS_2$ and Cu_3P–GDY, respectively; (c) is the GMM-10 SEM diagram of the composite catalyst; (d) electron transmission diagram and EDX diagram of the CGM-10 composite catalyst; (e) ICP test results for $Mo_{0.1}NiS_2$; (f) CGM-10 HRTEM image; and (g) diffraction rings of CGM-10.

Published on 27 Januwari 2025. Downloaded on 5/28/2026 5:22:55 AM.

adsorption of water molecules and promote the reaction to occur in the positive direction. A lattice spacing of 0.2385 nm is discernible, corresponding to the (202) crystallographic plane of Cu_3P–GDY. The (311) and (321) crystal faces of $Mo_{0.1}NiS_2$ and the (311) crystal faces of Cu_3P can be observed from the diffraction ring in Fig. 3(g). It is also proved that CMM-10 is a kind of polycrystalline catalyst.

3.2. Hydrogen evolution performance of photocatalysts

All hydrogen evolution experiments were performed using TEOA as a sacrificial reagent and under the irradiation of a 5 W analog lamp to evaluate the photocatalyst performance. As depicted in Fig. 4(a), the composite catalyst exhibited superior hydrogen evolution performance compared to the single catalyst. This may be due to the low hydrogen evolution due to the faster-photogenerated carrier recombination rate and the scarcity of active sites of the single catalyst. The composite catalyst CGM-10 achieved a hydrogen evolution rate of approximately 133.1 μmol g^{-1}, which is notably 4.7 and 2.9 times higher than that of Cu_3P–GDY and $Mo_{0.1}NiS_2$, respectively. Fig. 4(b) explores the influence of different doping ratios of Mo on hydrogen evolution, and it is found that the hydrogen evolution effect is best when the doping ratio is 10%. Fig. 4(c) examines how different proportions of the cocatalyst Cu_3P–GDY affect the composite photocatalyst's hydrogen evolution activity. The results indicated that when Cu_3P–GDY was composited with $Mo_{0.1}NiS_2$ in different ratios, there was a tendency for an initial increase followed by a subsequent decrease. The optimal hydrogen evolution activity was observed when the ratio of Cu_3P–GDY to $Mo_{0.1}NiS_2$ reached 1 : 10. This may be attributed to the fact that an excess of Cu_3P–GDY may obstruct the active sites of $Mo_{0.1}NiS_2$, impeding the composite photocatalyst's light absorption.[33] Considering that TEOA, the sacrificial reagent, is an alkaline solution, Fig. 4(d) explores the effect of different pH values on hydrogen evolution activity. The optimal hydrogen yield is achieved at a pH of 9, possibly due to the reduced availability of free protons in a strongly basic environment. In contrast, in a weakly basic environment, TEOA is more likely to become protonated.[34] In addition to the activity of the photocatalyst, the stability of the catalyst is also a key factor for the photocatalyst in practical applications. As shown in Fig. 4(e), the composite catalyst exhibited excellent stability after repeated cycles of 20 h (5 h per cycle, 4 cycles in total, with an additional 9 mg of EY added to the first and third cycles). The

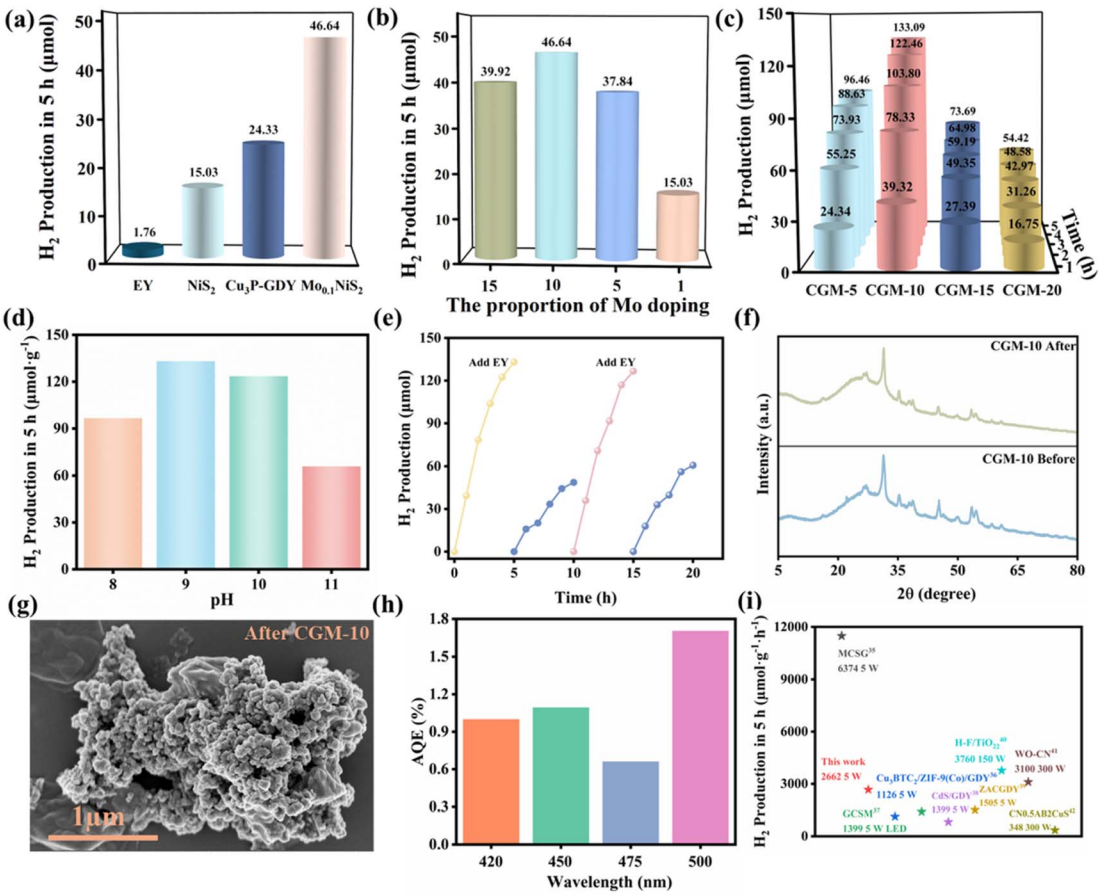

Fig. 4 Photocatalytic hydrogen evolution rates of (a) EY, Cu_3P–GDY, NiS_2 and $Mo_{0.1}NiS_2$ and (b) Mo_xNiS_2 (x = 0.01, 0.05, 0.1, 0.2) under 5 W simulated light irradiation; (c) different proportions of Cu_3P–GDY recombination to $Mo_{0.1}NiS_2$; (d) hydrogen evolution of the complex catalyst CGM-10 in different acid–base environments; (e) stable cycle test of composite catalyst CGM-10 within 20 h; (f) XRD patterns of CGM-10 before and after hydrogen production; (g) SEM patterns of CGM-10 after hydrogen production; (h) AQE chart of CGM-10; and (i) comparison of the catalytic activity of CGM-10 with reported catalysts.

 This journal is © The Royal Society of Chemistry 2025

Published on 27 Januwari 2025. Downloaded on 5/28/2026 5:22:55 AM.

hydrogen precipitation performance of the third cycle was found to be 95% of that of the first cycle. By comparing XRD (Fig. 4(f)) and SEM (Fig. 4(g)) data before and after hydrogen production, it was found that the internal structure of CGM-10 did not change significantly. This provides convincing evidence of the catalyst's stability. Fig. 4(h) illustrates the quantum efficiency of the composite catalyst, as determined under monochromatic illumination. The composite catalyst CGM-10 displays the highest photocatalytic activity, with an AQE of 1.70% at 550 nm, as evidenced by the measurements. In order to provide a comprehensive comparison of the performance of similar catalysts, a comparison is presented in Fig. 4(i).[35–42]

3.3. Factors affecting photocatalytic activity

In order to investigate the stability and dispersion of the chemical agent, electrophoretic tests were conducted in order to observe the surface potential of the catalyst. The positive and negative values of the zeta potential exert an influence on the absorbability of particles. When the potential is negative, there is an increase in the number of negative charges on the surface of the particles, which enhances the adsorption of positively charged ions.[43,44] Fig. 5(a) illustrates that the potential of CGM-10 is more negative than that of Cu_3P–GDY and $Mo_{0.1}NiS_2$, which is more conducive to H^+ adsorption on the surface of the composite catalyst. Furthermore, the composite catalyst displays enhanced stability and more uniform dispersion.

The adsorption performance of photocatalysts can be evaluated through the use of nitrogen adsorption–desorption isotherms. As illustrated in Fig. 5(b), $Mo_{0.1}NiS_2$, Cu_3P–GDY and CGM-10 exhibited H3-type hysteresis loops and IV-type adsorption isotherms.[45] A high pore size distribution and lack of connectivity were exhibited.[46] The pore size distribution curve in Fig. 5(c) was also obtained by the Brunauer–Emmett–Teller (BET) method, and the results demonstrated that the catalyst was a mesoporous material. The nano-mesoporous material facilitates light scattering between the pores, thereby enhancing the light absorption capacity of the catalyst.[47,48] The synthesis of the new composite material CGM-10 involved the loading of Cu_3P–GDY onto the $Mo_{0.1}NiS_2$ surface. This resulted in an increased specific surface area and the average pore diameter of CGM-10 to 23.3980 $m^2\ g^{-1}$ and 32.4911 nm (see Table 1), respectively. In comparison to the specific surface areas of 9 $m^2\ g^{-1}$ for $Mo_{0.1}NiS_2$ and 20 $m^2\ g^{-1}$ for Cu_3P–GDY, the enhanced specific surface area of CGM-10 can facilitate the generation of additional hydrogen evolution active sites.

Table 1 The specific surface area, pore volume and aperture parameters of Cu_3P–GDY, $Mo_{0.1}NiS_2$ and CGM-10

Samples	S_{BET} ($m^2\ g^{-1}$)	Pore volume × 10^{-3} ($cm^3\ g^{-1}$)	Average pore size (nm)
CGM-10	23	0.19	32
$Mo_{0.1}NiS_2$	9	0.04	18
Cu_3P–GDY	20	0.11	21

The efficient photocatalytic reaction must satisfy both thermodynamic and kinetic conditions.[49] The UV-visible absorption spectrum of the catalyst can be observed in Fig. 6(a). The results show that the composite catalyst CGM-10 has a high absorption intensity. It can be observed that the utilization of sunlight by the catalyst increases with the increase of absorption intensity. It can be concluded that the utilization of solar energy by CGM-10 is higher than those of Cu_3P–GDY and $Mo_{0.1}NiS_2$.[50]

Due to the migration of the photogenerated carriers during the catalyst reaction, the separation efficiency of photogenerated carriers can be measured by steady-state fluorescence. Typically, the fluorescence intensity of the photogenerated carriers is proportional to the recombination rate, whereby a higher recombination rate of the photogenerated carriers results in a lower electron utilization rate of the catalyst.[51] Consequently, the fluorescence intensity of various catalysts was evaluated, as illustrated in Fig. 6(b). It was observed that the catalyst exhibited the most pronounced PL peak at approximately 542 nm. In comparison to $Mo_{0.1}NiS_2$, the fluorescence intensity of CMM-10 was found to be significantly diminished. The charge-directed transfer between Cu_3P–GDY and $Mo_{0.1}NiS_2$ can facilitate the efficient utilization of photogenerated carriers. Time-resolved photoluminescence spectra (TRPL) can reflect the average carrier lifetime of each catalyst, as shown in Fig. 6(c). The average lifetimes of $Mo_{0.1}NiS_2$, Cu_3P–GDY and CGM-10 are 1.18, 1.21 and 1.09 ns, respectively, based on the kinetics of the decay spectra, as shown in Table 2. A shorter lifetime indicates a higher separation efficiency of the catalyst.

Often in the photocatalytic hydrogen evolution kinetics, the carrier separation and transport characteristics play a decisive role. Therefore, the density of carriers, charge transfer capacity and hydrogen evolution capacity were investigated by

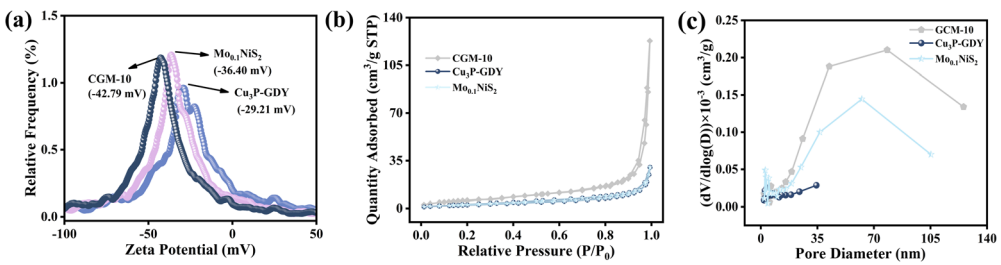

Fig. 5 (a) Zeta potential diagram of the catalyst; (b) nitrogen adsorption–desorption isotherms and (c) pore size distribution of Cu_3P–GDY, $Mo_{0.1}NiS_2$ and CGM-10.

Published on 27 Januwari 2025. Downloaded on 5/28/2026 5:22:55 AM.

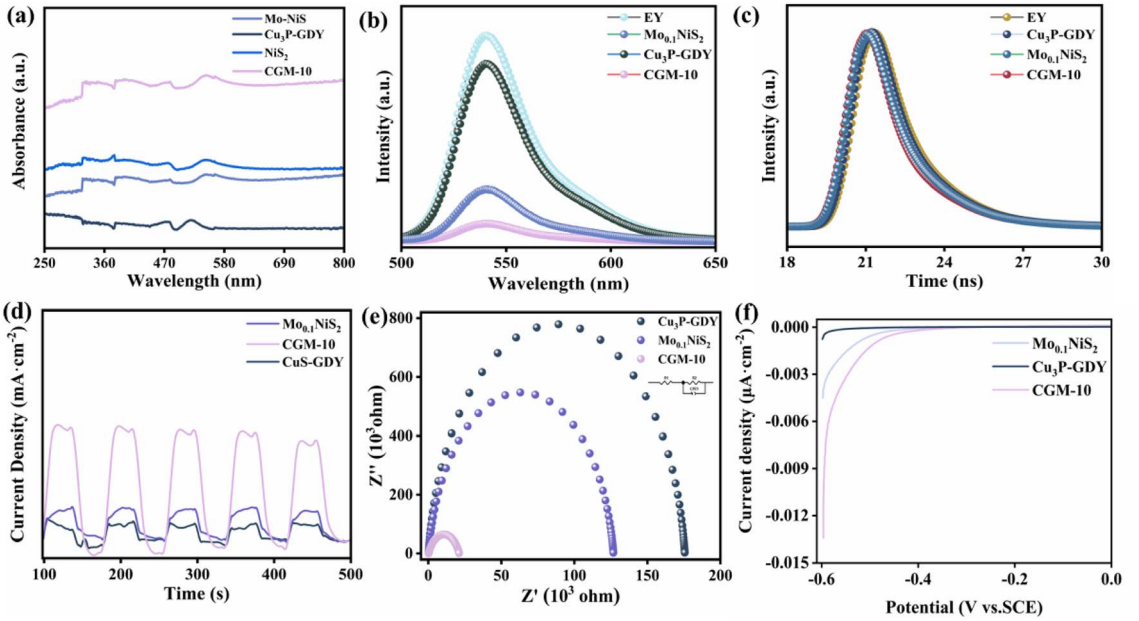

Fig. 6 (a) UV-vis diffuse reflectance curves of NiS_2, $Mo_{0.1}NiS_2$, Cu_3P–GDY and CMM-10; (b) PL, (c) TRPL, (d) IT curve, (e) EIS curve of $Mo_{0.1}NiS_2$, Cu_3P–GDY and CGM-10; and (f) LSV curve for $Mo_{0.1}NiS_2$, Cu_3P–GDY and CGM-10 measured in a dark state.

Table 2 The exponential curve fitted parameters of emission decay for catalysts

System	Lifetime, τ (ns)	Pre-exponential factors A (%)	Average lifetime $\langle\tau\rangle$ (ns)	χ^2
EY	$\tau_1 = 1.24$	$A_1 = 100$	1.24	1.52
Cu_3P–GDY	$\tau_1 = 1.17$	$A_1 = 96.75$	1.20	1.38
	$\tau_2 = 6.62$	$A_2 = 3.25$		
$Mo_{0.1}NiS_2$	$\tau_1 = 1.15$	$A_1 = 94.85$	1.18	1.19
	$\tau_2 = 3.02$	$A_2 = 5.15$		
CGM-10	$\tau_1 = 0.91$	$A_1 = 63.38$	1.09	1.20
	$\tau_2 = 1.69$	$A_2 = 36.17$		

photocurrent response, EIS and LSV. The photocurrent response can often reveal the separation of photogenerated charge carriers during hydrogen evolution.[52] As illustrated in Fig. 6(a), the photocurrent response density of the composite photocatalyst CMG-10 is considerably higher than that of $Mo_{0.1}NiS_2$. This superior electron transport capability of Cu_3P–GDY aids in the efficient migration of photogenerated holes and electrons.[53] Fig. 6(e) is the EIS diagram after fitting through the equivalent circuit. As shown in the figure, the diameter of the composite catalyst CGM-10 is the smallest, which indicates that the resistance of charge transfer of the composite catalyst is small. Fig. 6(f) shows the LSV curve of the catalyst. The results show that the composite catalyst exhibits the smallest hydrogen evolution potential at a given current density, indicative of its commendable charge separation ability.[54]

3.4. Analysis of the electronic structure of photocatalysts

XPS and *in situ* XPS are techniques for examining the chemical composition, valence state and electron transfer at the heterojunction interface of the catalyst. From the total XPS spectrum, it can be observed that Fig. 7a(III) contains all the elements of Cu_3P–GDY (Fig. 7a(I)) and $Mo_{0.1}NiS_2$ (Fig. 7a(II)), indicating that the CGM-10 was successfully prepared. Fig. 7b(I) shows the C 1s XPS fine spectrum of catalyst CuS–GDY, with four peaks at the binding energy of 284.26, 284.92, 285.73, and 288.71 eV, corresponding to C=C(sp^2), C≡C (sp), C–O, and C=O, respectively. Fig. 7c reveals that the fine spectrum of Cu 2p is assigned to Cu $2p_{3/2}$ and $2p_{1/2}$. Peaks at 933.41 and 953.16 eV correspond to Cu^{2+} in Cu_3P, whereas peaks at 932.36 and 952.13 eV correspond to Cu^{+}.[55] Meanwhile, Fig. 7d–f explore the elemental composition of $Mo_{0.1}NiS_2$. The results of Fig. 7d show that two spin–orbit peaks of Mo $3d_{5/2}$ (Mo^{4+}) and $3d_{3/2}$ (Mo^{3+}) are observed by Mo 3d fine spectrum.[56] From Fig. 7f, it can be observed that the satellite peaks of the mixed oxidation states of Ni^{2+} and Ni^{3+} surface ions are also found.[57,58] The fine spectrum of S 2p corresponds to S $2p_{3/2}$.[59,60] The shift of the binding energy of the elements means that the intrinsic charge migrates after contact with the catalyst. In general, if the movement in the direction of lower binding energy indicates the charge input, the opposite indicates the charge output. Consequently, upon contact between Cu_3P–GDY and $Mo_{0.1}NiS_2$, the binding energy is transferred. A comparison of dark state Fig. 7(I) and (II) reveal that Cu_3P–GDY gains electrons, with the binding energy moving in a smaller direction. In contrast, the binding energy of $Mo_{0.1}NiS_2$ exhibits an upward shift, indicating a loss of electrons. In the majority of cases, the occurrence of photocatalytic reactions will result in the migration of photogenerated carriers under the influence of light, which will consequently impact the alteration in binding energy. The effect of illumination on the binding energy of CGM-10 was therefore investigated using *in situ* XPS. The comparison between CGM-10 in the dark state (Fig. 7(II)) and illumination (Fig. 7(III))

 This journal is © The Royal Society of Chemistry 2025

Published on 27 Januwari 2025. Downloaded on 5/28/2026 5:22:55 AM.

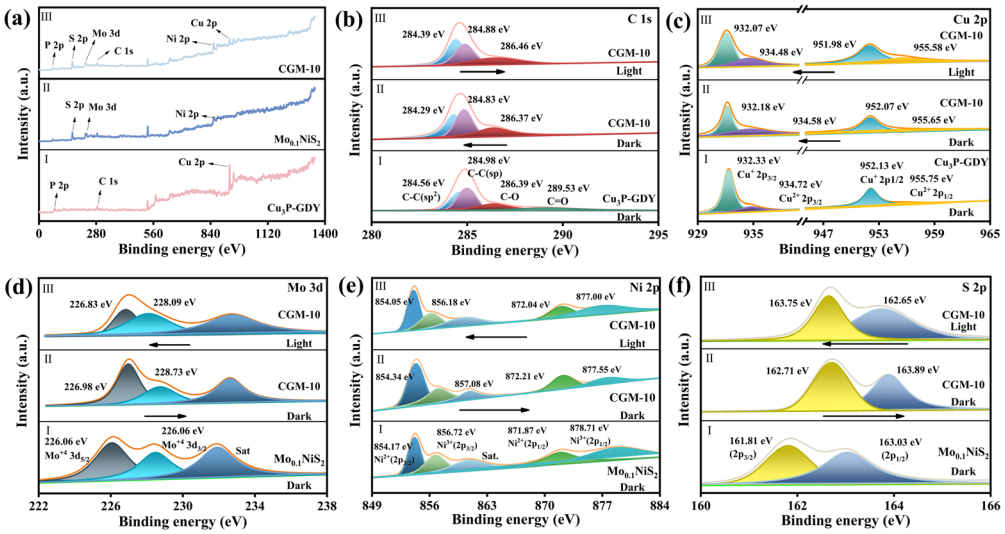

Fig. 7 (a) Total XPS spectra of Cu_3P–GDY, $Mo_{0.1}NiS_2$ and CGM-10; fine XPS spectra of (b) C 1s, (c) Cu 2p, (d) Mo 3d, (e) Ni 2p and (f) S 2p in dark states (I and II) and under light (III).

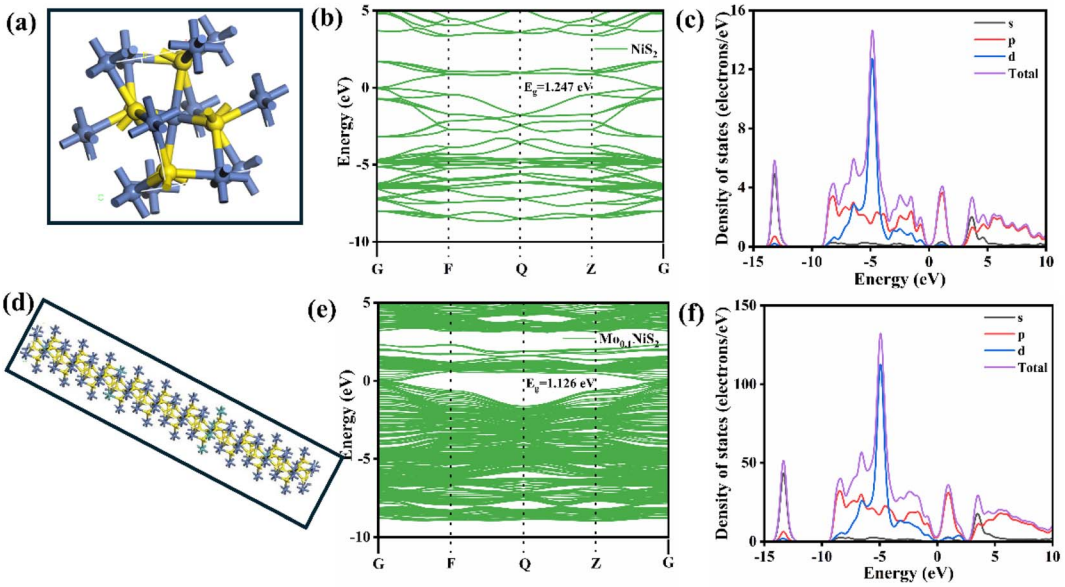

Fig. 8 (a) Structural model and (b) band structure and (c) state density of NiS_2; (d) structural model and (e) band structure and (f) state density of Mo doping in NiS_2.

demonstrates that the binding energy of C shifts in a larger direction, indicating that C loses electrons following illumination.[61] Following illumination, all elements, including Cu, Mo, Ni and S, exhibited an increase in the electron gain, resulting in a notable shift in the binding energy.

When the element is doped, the crystal structure will change. Fig. 8(a) shows the crystal structure of undoped NiS_2, while Fig. 8(d) explores the effect of 10% Mo element on the photoelectric properties of NiS_2. The band structure and state density of NiS_2 and $Mo_{0.1}NiS_2$ are calculated by the first principles of DFT. From Fig. 8(b), it can be found that the conduction band bottom and valence band top of NiS_2 are located at the *Z* point at the same time, which indicates that NiS_2 is a direct bandgap semiconductor with a band gap of 1.247 eV.[62] However, when no intermediate energy level is introduced between the conduction band (CB) and valence band (VB) after Mo element doping, the jump type is still a direct jump.[63] However, the band gap of $Mo_{0.1}NiS_2$ is reduced to 1.126 eV, and the energy difference from 0.44 to 0.68 eV after doping to the Fermi level is increased. This may be due to an increase in the optical band gap caused by the Burstein–Moss shift effect.[64] The optical band gap is the energy difference between the Fermi level and the VB. At the same time, the band line of $Mo_{0.1}NiS_2$ also becomes denser, which also indicates that the electron state density of $Mo_{0.1}NiS_2$ is higher.

Published on 27 Januwari 2025. Downloaded on 5/28/2026 5:22:55 AM.

This is consistent with the results in Fig. 8(f), indicating that $Mo_{0.1}NiS_2$ has a high electronic conductivity. From Fig. 8(e) and (f), it is observed that the electron energy contribution of Mo doped does not change the VB.

The electronic structures of GDY and Cu_3P are calculated by density functional theory based on first principles. Fig. 9(a) and (d) show the structure of GDY (002) and Cu_3P (211) after structural optimization, respectively. Fig. 9(b) illustrates that GDY is a direct band gap. Nevertheless, electrons are subject to their own forces as a consequence of electron self-interaction, which gives rise to an underestimation of the band gap in GGA calculations. Furthermore, the band gap results are also affected by the deficiencies inherent to the derivative discontinuity of the GGA functional itself. Consequently, the theoretical band gap (0.513 eV) is considerably lower than the actual band gap.[65,66] It can be seen from Fig. 9(c) that the CB and VB of GDY are mainly contributed by the p orbital.[67] Fig. 9(e) and (f) illustrate the band structure and state density diagram of Cu_3P, respectively. These results demonstrate that Fermi-level interleaving occurs in Cu_3P, which is indicative of the metal-like catalytic properties of this compound. Generally, metal-like catalysts have strong electrical conductivity and electron absorption ability, so Cu_3P can be used as the active site in the composite catalyst, thereby promoting the amount of hydrogen evolution under light.[68]

Fig. 10(a)–(c) show the calculated work functions of GDY, Cu_3P and $Mo_{0.1}NiS_2$ as 5.64, 4.00 and 4.49 eV, respectively. Often the magnitude of the work function represents the ability of the electrons to bond. When the work function is larger, it indicates that the electron binding ability is stronger, so the charge on the surface of the catalyst is efficiently utilized to participate in the reduction reaction of the hydrogen evolution process.[69] Usually, the difference between the work functions represents the potential difference between the semiconductors, which causes a driving force to form between the catalysts, thus facilitating the transfer of electrons between them. This is also one of the necessary conditions for the heterojunction formation.[70]

The mechanism of the performance enhancement of the composite photocatalyst CGM-10 was explored by UV-visible diffuse reflectance absorption spectroscopy and the Mott–Schottky test. The band gap of the catalyst can be obtained based on the conversion relationship between the Kubelka–Munk function and light energy. The band gap of NiS_2 is 1.62 eV, as illustrated in Fig. 10(d). Upon doping the elemental Mo into NiS_2, the band gap of Mo–NiS_2 decreases to 1.48 eV (as shown in Fig. 10(e)). A reduction in the band gap is conducive to carrier migration, which is more conducive to the redox reaction. As illustrated in Fig. 10(f), the band gap of Cu_3P is 0.6 eV. Fig. 10(g) and (h) are Mott–Schottky plots of GDY and $Mo_{0.1}NiS_2$ at 1000 (frequency) and 1500, respectively. The results show that the slopes of both plots are negative, thus it can be determined that GDY and $Mo_{0.1}NiS_2$ are n-type semiconductors. The flat-band potentials of both GDY and $Mo_{0.1}NiS_2$ measured with a calomel electrode as the reference electrode are −0.47 and −0.67 V, respectively. In general, the conduction band of n-type semiconductors is more negative than the flat band potential of 0.2 eV.[71] Therefore, the conduction positions of GDY and $Mo_{0.1}NiS_2$ are 0.67 and −0.87 V *vs.* SCE, respectively. According to the relation between the VB and the band gap ($E_{VB} = E_{CB} + E_g$), the VB position of GDY and $Mo_{0.1}NiS_2$ can be obtained as 0.41 and 0.86 V *vs.* SCE, respectively. The results show that GDY and $Mo_{0.1}NiS_2$ have interbank heterojunction structures. The relationship between the calculated work functions finally gives the band structure, as shown in Fig. 10(i).

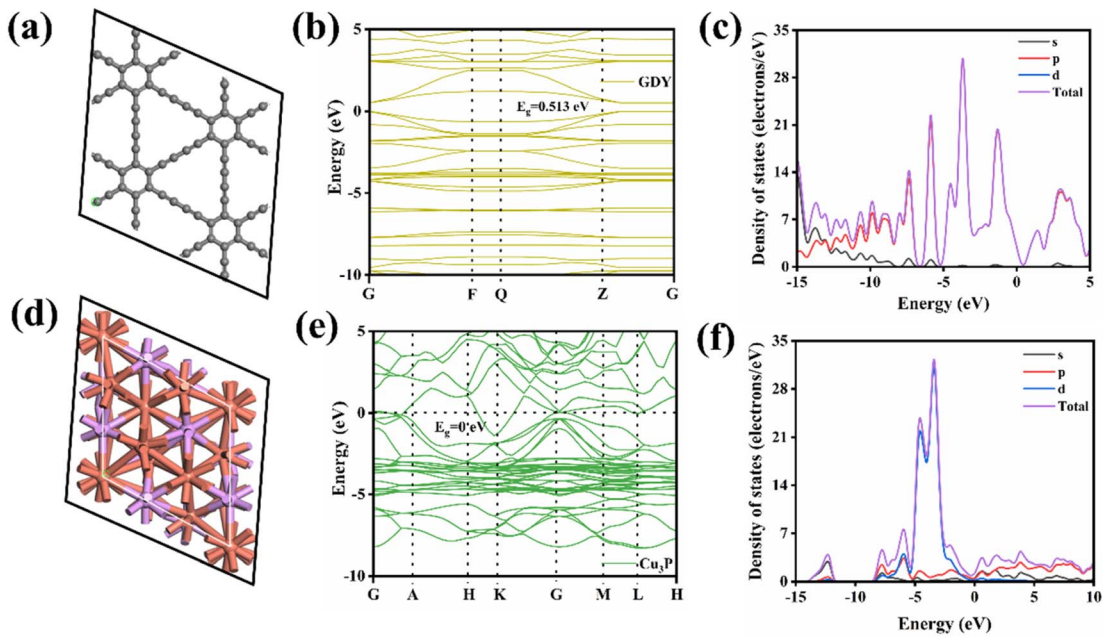

Fig. 9 (a) Structure model, (b) band structure and (c) state density of GDY; (d) structure model, (e) band structure and (f) state density of Cu_3P.

 This journal is © The Royal Society of Chemistry 2025

Published on 27 Januwari 2025. Downloaded on 5/28/2026 5:22:55 AM.

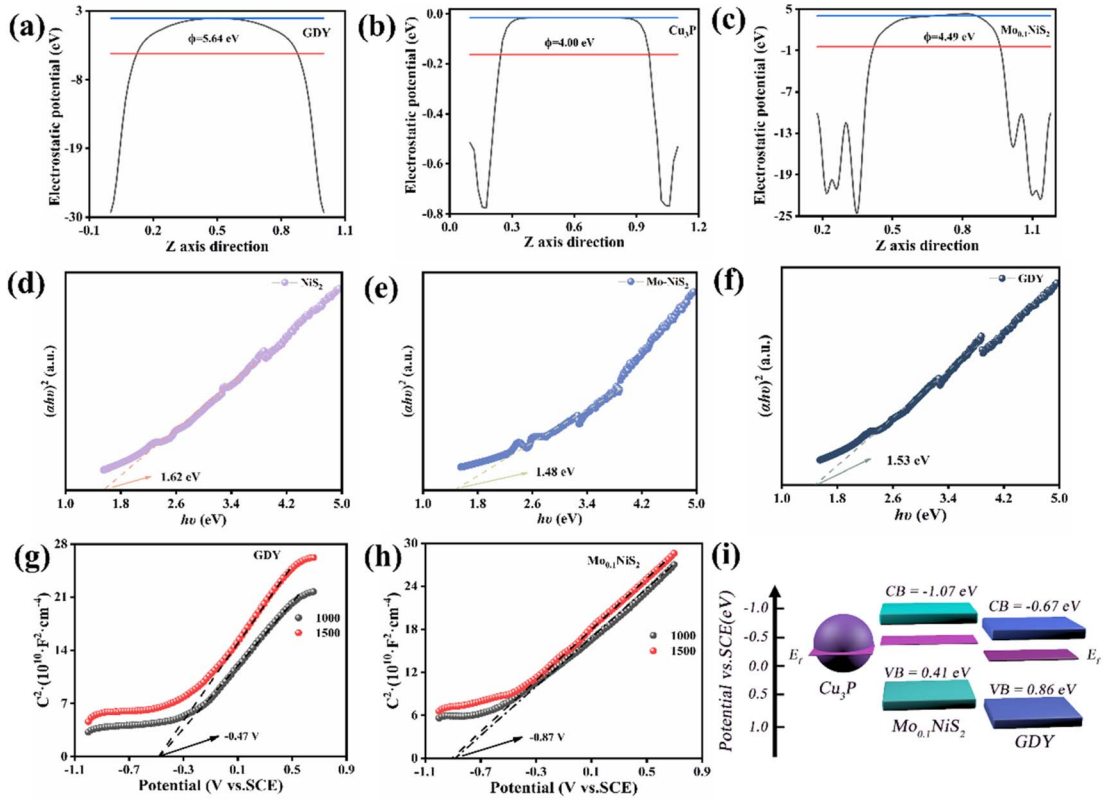

Fig. 10 Work functions of (a) GDY, (b) Cu_3P and (c) $Mo_{0.1}NiS_2$; bandgap structure diagram of (d) NiS_2, (e) $Mo_{0.1}NiS_2$ and (f) GDY; Mott–Schottky plots of (g) GDY and (h) $Mo_{0.1}NiS_2$ at different frequencies; and (i) band structure diagram between CGM-10.

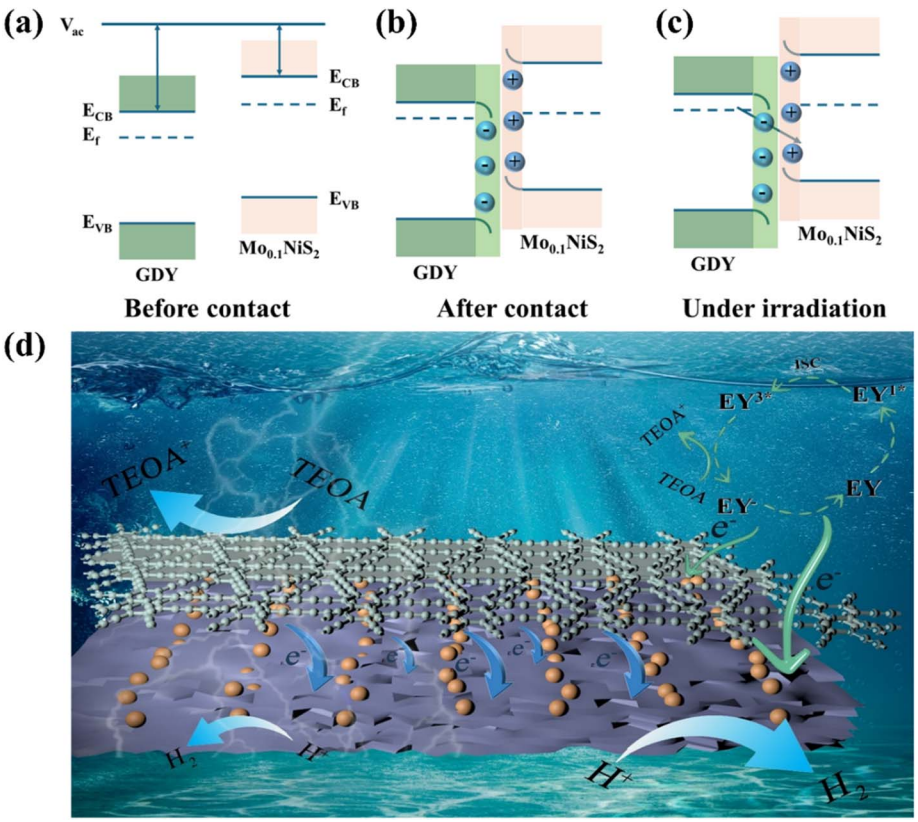

Fig. 11 (a–c) Schematic diagram of charge transfer mechanism between CGM-10; and (d) diagram of the mechanism of H_2 evolution in sunlight.

Published on 27 Januwari 2025. Downloaded on 5/28/2026 5:22:55 AM.

3.5. Possible mechanism

Based on the energy band structure and *in situ* XPS and DFT calculations, a possible mechanism for improving the performance of CGM-10 is proposed. Fig. 11(a) shows the band structure of the semiconductor before contact. The difference between the VB and the work function makes electron transfer possible.[72,73] Therefore, when GDY is in contact with $Mo_{0.1}NiS_2$, the Fermi level tends to be balanced due to the potential difference between the Fermi levels, which will cause electrons to escape from the Fermi level.[74] The transfer of electrons causes an internal electric field within GDY and $Mo_{0.1}NiS_2$. As shown in Fig. 11(c), when the photogenerated charge carrier of the semiconductor is excited under light, the photogenerated electrons will be removed from the semiconductor under the action of the internal electric field. Instead, photoluminescent holes are removed from $Mo_{0.1}NiS_2$ to Cu_3P.[75,76] Meantime, Cu_3P as a cocatalyst showed metal-like properties.[77] Therefore, Cu_3P exists as the active site for hydrogen evolution in the composite catalyst, which helps to provide more active sites for the catalyst and accelerate the migration of photogenerated carriers.

When the composite catalyst CGM-10 is irradiated by light, the photogenerated carrier is excited. Due to the internal electric field and Coulomb force generated inside the semiconductor, the photogenerated electrons produced by CB in GDY will be combined with the photogenerated holes produced by VB in $Mo_{0.1}NiS_2$ under the action of the two driving forces.[78] The photogenerated electrons produced by CB in GDY will combine with the photogenerated holes produced by VB in $Mo_{0.1}NiS_2$. GDY will leave strong oxidizing potholes in VB to oxidize TEOA. The photogenerated electrons of CB left behind in $Mo_{0.1}NiS_2$ will reduce H^+ to H_2.[79] Cu_3P, as a metalloid hydrogen evolution site, will attract some electrons on CB of $Mo_{0.1}NiS_2$ to transfer. Thus, the recombination rate of the photogenerated carriers will be reduced.[80] At the same time, EY was adsorbed on the surface of CGM-10 as a dye molecule. Under light exposure, the excited state EY^{1*} is formed, which is subsequently converted to the more stable EY^{3*}. Under the action of TEOA, EY^{3*} is reduced and quenched to EY^-. EY^-, which has strongly reduced power, reduces H^+ to H_2. Eventually, the dye molecules will return to their ground state.

4. Conclusions

In summary, we changed the crystal structure of NiS_2 through the element doping strategy, optimized the electron state density of $Mo_{0.1}NiS_2$, and thus improved the electron conductivity. Therefore, the conductivity of cocatalyst Cu_3P–GDY was stimulated to improve the hydrogen evolution performance. The results showed that the hydrogen evolution performance of NiS_2 doped with Mo was 3.1 times that of NiS_2, and the hydrogen evolution performance was improved 2.9 times to 133.1 μmol g^{-1} after loading the co-catalyst. At the same time, combining *in situ* XPS with UV, Mott–Schottky and work function analyses, the stepped heterojunction between CGM-10 was constructed to form a directional electron transport channel, which accelerates the separation of the photogenerated carriers and improves the hydrogen evolution performance. This work proves that the combination of organic catalysts with high conductivity and electronic conductivity can effectively improve the performance of the photocatalytic hydrogen evolution.

Data availability

Data are available from the authors upon request.

Author contributions

Jieyuan Du and Fei Jin designed the experiments and wrote the paper; Jieyuan Du performed the experiments; Youji Li, Zhiliang Jin and Guoping Jiang provided reagents, materials and analysis tools.

Conflicts of interest

The authors declare that they have no competing interests.

Acknowledgements

This work is financially supported by the Natural Science Foundation of Ningxia Province (2024AAC05053) and the Graduate Innovation Project of North Minzu University (YCX24394).

References

1 L. Yang, X. Li, G. Zhang, P. Cui, X. Wang, X. Jiang, J. Zhao, Y. Luo and J. Jiang, *Nat. Commun.*, 2017, **8**, 16049.
2 M. Cai, Y. Wei, Y. Li, X. Li, S. Wang, G. Shao and P. Zhang, *EcoEnergy*, 2023, **1**, 248–295.
3 S. Jin, H. Jing, L. Wang, Q. Hu and A. Zhou, *J. Adv. Ceram.*, 2022, **11**, 1431–1444.
4 H. Zhang, Z. Zhou, Y. Yin, H. Xu, Y. Wang, K. Yang, Z. Zhang, J. Wang and X. He, *EcoEnergy*, 2023, **1**, 217–247.
5 X. Wang, B. Liu, S. Ma, Y. Zhang, L. Wang, G. Zhu, W. Huang and S. Wang, *Nat. Commun.*, 2024, **15**, 2600.
6 Z. Liu, Y. Li and Z. Jin, *J. Mater. Chem. C*, 2023, **11**, 9327–9340.
7 D. Ma, J. Chen, J. Li, X. Ji and J.-W. Shi, *J. Mater. Chem. A*, 2024, **12**, 12293–12324.
8 B. Yan, Y. He and G. Yang, *J. Mater. Chem. A*, 2022, **10**, 1899–1908.
9 X. Zheng, Y. Yang, Y. Song, Z. Ma, Q. Gao, Y. Liu, J. Li, X. Wu, X. Wang, W. Mao, W. Liu, Y. Shen and X. Tian, *Interdiscip. Mater.*, 2023, **2**, 669–688.
10 T. Li, L. Zhang, X. Li, X. Wang and Z. Jin, *Nat. Sci.*, 2023, **36**(2), 25–34+42.
11 R. Yang, Y. Fan, Y. Zhang, L. Mei, R. Zhu, J. Qin, J. Hu, Z. Chen, Y. H. Ng, D. Voiry, S. Li, Q. Lu, Q. Wang, J. C. Yu and Z. Zeng, *Angew. Chem., Int. Ed.*, 2023, **62**, e202218016.
12 G. Du, Y. Fan, L. Jia, Y. Wang, Y. Hao, W. Zhao, Q. Su and B. Xu, *Front. Chem. Sci. Eng.*, 2023, **17**, 1707–1717.
13 Z. Jin, *J. Chin. Ceram. Soc.*, 2023, **51**(1), 106–116.
14 S. A. Gregory, A. K. Menon, S. Ye, D. S. Seferos, J. R. Reynolds and S. K. Yee, *Adv. Energy Mater.*, 2018, **8**, 1802419.

 This journal is © The Royal Society of Chemistry 2025

Published on 27 Januwari 2025. Downloaded on 5/28/2026 5:22:55 AM.

15 Z. Yu, H. Yan, C. Wang, Z. Wang, H. Yao, R. Liu, C. Li and S. Ma, *Front. Chem. Sci. Eng.*, 2023, **17**, 437–448.
16 J. Li, X. Gao, Z. Li, J.-H. Wang, L. Zhu, C. Yin, Y. Wang, X.-B. Li, Z. Liu, J. Zhang, C.-H. Tung and L.-Z. Wu, *Adv. Funct. Mater.*, 2019, **29**, 1808079.
17 X. Chen, X. Zheng, C. Zhang, D. Zhang, Y. Gao, S. Chen, Y. Xue and Y. Li, *Nano Energy*, 2023, **114**, 108622.
18 X. Zheng, S. Chen, J. Li, H. Wu, C. Zhang, D. Zhang, X. Chen, Y. Gao, F. He, L. Hui, H. Liu, T. Jiu, N. Wang, G. Li, J. Xu, Y. Xue, C. Huang, C. Chen, Y. Guo, T. B. Lu, D. Wang, L. Mao, J. Zhang, Y. Zhang, L. Chi, W. Guo, X.-H. Bu, H. Zhang, L. Dai, Y. Zhao and Y. Li, *ACS Nano*, 2023, **17**, 14309–14346.
19 S. Ding, J. Duan and S. Chen, *EcoEnergy*, 2024, **2**, 45–82.
20 J. Yu, Y. Yang, Y. Li, C. Cao and W. Song, *Nano Res.*, 2024, **17**, 2223–2233.
21 X. Zheng, Y. Xue, S. Chen and Y. Li, *EcoEnergy*, 2023, **1**, 45–59.
22 J. He, S. Y. Ma, P. Zhou, C. X. Zhang, C. He and L. Z. Sun, *J. Phys. Chem. C*, 2012, **116**, 26313–26321.
23 L. Guo, J. Gao, M. Li, Y. Xie, H. Chen, S. Wang, Z. Li, X. Wang and W. Zhou, *EcoEnergy*, 2023, **1**, 437–447.
24 X. Li, C. Zhao, J. Wang, J. Zhang, Y. Wu and Y. He, *Front. Chem. Sci. Eng.*, 2023, **17**, 1412–1422.
25 T. Wang and Z. Jin, *Results Surf. Interfaces*, 2024, **14**, 100188.
26 L. Ding, M. Lei, T. Wang, J. Wang and Z. Jin, *Carbon Lett.*, 2024, **34**, 2099–2112.
27 Y. Fan, X. Hao, J. Wang, Z. Hu and Z. Jin, *Surf. Interfaces*, 2023, **42**, 103512.
28 Q. Chang, X. Fu, J. Gao, Z. Zhang, X. Liu, C. Huang and Y. Li, *Adv. Mater.*, 2023, **35**, 2305317.
29 X. Fu, F. He, J. Gao, X. Yan, Q. Chang, Z. Zhang, C. Huang and Y. Li, *J. Am. Chem. Soc.*, 2023, **145**, 2759–2764.
30 D. Zhou, X. Xue, X. Wang, Q. Luan, A. Li, L. Zhang, B. Li, W. Dong, G. Wang and C. Hou, *Appl. Catal., B*, 2022, **310**, 121337.
31 J. Liu, G. Hodes, J. Yan and S. F. Liu, *Chin. J. Catal.*, 2021, **42**, 205–216.
32 C. Zhuang, Y. Chang, W. Li, S. Li, P. Xu, H. Zhang, Y. Zhang, C. Zhang, J. Gao, G. Chen, T. Zhang, Z. Kang and X. Han, *ACS Nano*, 2024, **18**, 5206–5217.
33 R. Guan, L. Wang, D. Wang, K. Li, H. Tan, Y. Chen, X. Cheng, Z. Zhao, Q. Shang and Z. Sun, *Chem. Eng. J.*, 2022, **435**, 135138.
34 C. Yang, X. Li and Z. Jin, *Sci. China Mater.*, 2024, **67**, 493–503.
35 Z. Fan, X. Guo, M. Yang and Z. Jin, *Chin. J. Catal.*, 2022, **43**, 2708–2719.
36 F. Jin, B. Yang, X. Wang, T. Li, N. Tsubaki and Z. Jin, *Chin. J. Struct. Chem.*, 2023, **42**, 100198.
37 M. Li, J. Z. Wang and Z. L. Jin, *Rare Met.*, 2024, **43**, 1999–2014.
38 J. X. Lv, Z. M. Zhang, J. Wang, X. L. Lu, W. Zhang and T. B. Lu, *ACS Appl. Mater. Interfaces*, 2019, **11**, 2655–2661.
39 T. Wang and Z. Jin, *J. Mater. Sci. Technol.*, 2023, **155**, 132–141.
40 Q. Gao, F. Si, S. Zhang, Y. Fang, X. Chen and S. Yang, *Int. J. Hydrogen Energy*, 2019, **44**, 8011–8019.
41 H. Che, L. Xiao, W. Zhou, Q. Zhou, H. Li, P. Hu, J. Wang, X. Chen and H. Wang, *J. Alloys Compd.*, 2022, **896**, 162931.
42 R. Shen, J. Xie, P. Guo, L. Chen, X. Chen and X. Li, *ACS Appl. Energy Mater.*, 2018, **1**, 2232–2241.
43 X. Gao, A. Omosebi, J. Landon and K. Liu, *ECS Meet. Abstr.*, MA2015-01, 1212, 2015.
44 F. Netzer, A. P. Manian, T. Bechtold and T. Pham, *Cellulose*, 2024, **31**, 8501–8517.
45 X. Wang, Y. Li, T. Li and Z. Jin, *Adv. Sustainable Syst.*, 2023, **7**, 2200139.
46 M. G. Mohamed, M. H. Elsayed, C.-J. Li, A. E. Hassan, I. M. A. Mekhemer, A. F. Musa, M. K. Hussien, L.-C. Chen, K.-H. Chen, H.-H. Chou and S.-W. Kuo, *J. Mater. Chem. A*, 2024, **12**, 7693–7710.
47 Y. Ming, Z. Cheng, S. Shi, J. Su, W.-F. Io, H. Wu, J. Li and B. Fei, *Small*, 2024, **20**, 2309750.
48 C. Zheng, G. Jiang, Y. Li and Z. Jin, *J. Alloys Compd.*, 2022, **904**, 164041.
49 Y. Cao, H. Gou, P. Zhu and Z. Jin, *Chin. J. Struct. Chem.*, 2022, **41**, 79–85.
50 S.-Y. Yuan, T.-T. Li, J.-Y. Cui, J.-K. Sun, Y.-S. Gong, A. Braun, H. Liu and J.-J. Wang, *EcoEnergy*, 2024, **2**, 322–335.
51 Z. Jin, H. Li and J. Li, *Chin. J. Catal.*, 2022, **43**, 303–315.
52 Y. Dong, B. Wang, D. Xie, J. Lv, J. Cui, Z. Bao, G. Xu and W. Shen, *EcoEnergy*, 2024, **2**, 489–502.
53 X.-P. Wang, Z.-L. Jin and X. Li, *Rare Met.*, 2023, **42**, 1494–1507.
54 X. Wang, B. Liu, Y. Zhang, T. Butburee, K. K. Ostrikov, S. Wang and W. Huang, *EcoEnergy*, 2023, **1**, 108–153.
55 Z. Cai, D. Zhao, X. Fan, L. Zhang, J. Liang, Z. Li, J. Li, Y. Luo, D. Zheng, Y. Wang, T. Li, H. Yan, B. Ying, S. Sun, A. A. Alshehri, H. Yan, J. Xu, Q. Kong and X. Sun, *Small*, 2023, **19**, 2300620.
56 Y. Zhou, J. Zhang, H. Ren, Y. Pan, Y. Yan, F. Sun, X. Wang, S. Wang and J. Zhang, *Appl. Catal., B*, 2020, **268**, 118467.
57 B. Cong, X. Li and G. Chen, *Chem. Eng. J.*, 2023, **460**, 141713.
58 F. Song, G. Yang, L. Pan and Q. Chen, *Composites, Part B*, 2023, **267**, 111025.
59 Y. Zhang, W. Zhou, Y. Tang, Y. Guo, Z. Geng, L. Liu, X. Tan, H. Wang, T. Yu and J. Ye, *Appl. Catal., B*, 2022, **305**, 121055.
60 Y. Wu, P. Zhu, Y. Li, L. Zhang and Z. Jin, *ACS Appl. Energy Mater.*, 2022, **5**, 8157–8168.
61 B. Wang, K. Qian, W. Yang, W. An, L.-L. Lou, S. Liu and K. Yu, *Front. Chem. Sci. Eng.*, 2023, **17**, 1728–1740.
62 W. Zhou, L. Liu, M. Yuan, Q. Song and P. Wu, *Comput. Mater. Sci.*, 2012, **54**, 109–114.
63 S. Ahmed, T. Hasan, A. K. M. S. H. Faysal, S. S. Nishat, M. N. I. Khan, A. Kabir and I. Ahmed, *Comput. Mater. Sci.*, 2022, **214**, 111743.
64 J. Wang, D. Li, C. Xu, X. Yuan and P. Yang, *Superlattices Microstruct.*, 2020, **138**, 106387.
65 Z. Jin, C. Yang, L. Li and J. Jiang, *J. Ind. Eng. Chem.*, 2024, **142**, 449–462.
66 M. Luo, G. Jiang, M. Yu, Y. Yan, Z. Qin, Y. Li and Q. Zhang, *J. Mater. Sci. Technol.*, 2023, **161**, 220–232.
67 C. Yang, X. Li, M. Li, G. Liang and Z. Jin, *Chin. J. Catal.*, 2024, **56**, 88–103.

68 C. Zhuang, W. Li, Y. Chang, S. Li, Y. Zhang, Y. Li, J. Gao, G. Chen and Z. Kang, *J. Mater. Chem. A*, 2024, **12**, 5711–5718.
69 Z. Liu, F. Jin, X. Li, P. Zhang and Z. Jin, *J. Mater. Sci. Technol.*, 2024, **188**, 131–143.
70 R. Shen, N. Li, C. Qin, X. Li, P. Zhang, X. Li and J. Tang, *Adv. Funct. Mater.*, 2023, **33**, 2301463.
71 G. Jia, Y. Wang, X. Cui, H. Zhang, J. Zhao, L. H. Li, L. Gu, Q. Zhang, L. Zheng, J. Wu, Q. Wu, D. J. Singh, W. Li, L. Zhang and W. Zheng, *Matter*, 2022, **5**, 206–218.
72 D. Zhang, D. Zhang, F. Zhao, Y. Zhao, H. Li, J. Liu, X.-Y. Ji, X. Pu and H. Zhang, *J. Mater. Chem. A*, 2024, **12**, 33546–33558.
73 B. Xia, B. He, J. Zhang, L. Li, Y. Zhang, J. Yu, J. Ran and S.-Z. Qiao, *Adv. Energy Mater.*, 2022, **12**, 2201449.
74 Z. Zhou, H. Yao, Y. Wu, T. Li, N. Tsubaki and Z. Jin, *Acta Phys.-Chim. Sin.*, 2024, **40**, 2312010.
75 F. Li, G. Zhu, J. Jiang, L. Yang, F. Deng, Arramel and X. Li, *J. Mater. Sci. Technol.*, 2024, **177**, 142–180.
76 X. Li, Y. Li, X. Guo and Z. Jin, *Front. Chem. Sci. Eng.*, 2023, **17**, 606–616.
77 L. Zhang, Y. Wu, N. Tsubaki and Z. Jin, *Acta Phys.-Chim. Sin.*, 2023, **39**, 2302051.
78 L. Fan, X. Gou, L. Wang, Z. Jin and N. Tsubaki, *Front. Chem. Sci. Eng.*, 2024, **18**(12), 158.
79 Y. Wang, Y. Han, R. Zhao, J. Han and L. Wang, *Front. Chem. Sci. Eng.*, 2023, **17**, 1301–1310.
80 A. Meng, B. Cheng, H. Tan, J. Fan, C. Su and J. Yu, *Appl. Catal., B*, 2021, **289**, 120039.

Published on 27 Januwari 2025. Downloaded on 5/28/2026 5:22:55 AM.

This journal is © The Royal Society of Chemistry 2025